Research Article Vol. 10, No. 7 / 1 July 2020 / Optical Materials Express 1687
Optical Materials EXPRESS

Structure and morphology of low mechanical loss TiO_2-doped Ta_2O_5

MARIANA A. FAZIO,[1,5] GABRIELE VAJENTE,[2] ALENA ANANYEVA,[2] ASHOT MARKOSYAN,[3] RICCARDO BASSIRI,[3] MARTIN M. FEJER,[3] AND CARMEN S. MENONI[1,4]

[1]Department of Electrical and Computer Engineering, Colorado State University, Fort Collins 80521, USA
[2]LIGO Laboratory, California Institute of Technology, Pasadena 91125, USA
[3]Department of Applied Physics, Ginzton Laboratory, Stanford University, Stanford 94305, USA
[4]Carmen.Menoni@colostate.edu
[5]Mariana.Fazio@colostate.edu

Abstract: The exceptional stability required from high finesse optical cavities and high precision interferometers is fundamentally limited by Brownian motion noise in the interference coatings of the cavity mirrors. In amorphous oxide coatings these thermally driven fluctuations are dominant in the high index layer compared to those in the low index SiO_2 layer in the stack. We present a systematic study of the evolution of the structural and optical properties of ion beam sputtered TiO_2-doped Ta_2O_5 films with annealing temperature. We show that low mechanical loss in TiO_2-doped Ta_2O_5 with a Ti cation ratio = 0.27 is associated with a material that consists of a homogeneous titanium-tantalum-oxygen mixture containing a low density of nanometer sized Ar-filled voids. When the Ti cation ratio is 0.53, phase separation occurs leading to increased mechanical loss. These results suggest that amorphous mixed oxides with low mechanical loss could be identified by considering the thermodynamics of ternary phase formation.

1. Introduction

Amorphous oxide interference coatings take on a major role in visible and near infrared high finesse optical cavities and high precision interferometers in that mechanical damping in these materials arising from Brownian motion noise fundamentally limits their sensitivity [1,2]. The thermally driven fluctuations (thermal noise) lead to optical path length variations that affect frequency stabilization in optical clocks [3–5] and decrease the sensitivity of gravitational wave detectors such as Advanced LIGO [6] and Advanced Virgo [7]. Therefore there is a pressing need to understand the underlying processes that lead to mechanical dissipation in these materials.

These mechanical losses, as opposed to absorption or scattering losses, are related to the internal degrees of freedom in the material that makes up the coating. These losses can be quantified by the so-called mechanical loss angle of the material (ϕ), which is the ratio of the imaginary to real parts of the Young's modulus. In fact, the power spectrum of the thermal noise is proportional to the mechanical loss angle according to the fluctuation-dissipation theorem [8]. Furthermore, the loss angle is related to the dissipated power given that a fraction $2\pi\phi$ of the stored energy in the test mass is dissipated during each cycle [9].

In amorphous oxide thin film coatings used in near infrared high finesse cavities and interferometers the thermal noise is dominant in the high index layer, typically tantala (Ta_2O_5), compared to those in the low index silica (SiO_2) layer in the stack [10]. Currently there are two known processes that lead to a reduction in the mechanical losses of high index oxide coatings: post deposition thermal treatment (annealing) and doping. In the first case, annealing has been reported to significantly reduce the mechanical loss of the high index material in the reflective stack in addition to decreasing stress and optical absorption [11,12]. In particular for tantala films it has been found that annealing has the strongest effect on the reduction of the coating

#395503 https://doi.org/10.1364/OME.395503
Journal © 2020 Received 16 Apr 2020; revised 11 Jun 2020; accepted 11 Jun 2020; published 26 Jun 2020

Optical Materials EXPRESS

loss angle, even when films are grown at elevated substrate temperatures [13]. In the second case, it was found that by doping tantala with 20-25% of titania (TiO_2) the mechanical losses could be reduced by around 40% [6,14,15]. This led to designing the high reflectance mirrors in both Advanced LIGO and Advanced Virgo to be composed of alternating layers of silica and titania-doped tantala (TiO_2:Ta_2O_5). The thermal noise reduction achieved with this particular mixed oxide coating has contributed to an increased sensitivity of the observatories which was instrumental to recent major detections [16].

The causes of the reduction in mechanical loss achieved with titania doping and the role of the dopant concentration in the material mechanical loss are not yet understood. Harry *et. al.* evaluated films with different titania molecular concentrations up to 55% with all coatings subjected to annealing in air at 600°C, and reported that the mechanical loss reached a minimum for a specific dopant concentration of around 20% [17]. Several authors confirmed this decrease in mechanical loss as well [14,15,18–21]. There are however, only a few studies on the structure and properties of titania-doped tantala films and their relation to mechanical loss. Bassiri *et. al.* investigated structural modifications of titania-doped tantala using transmission electron microscopy for films with different Ti cation ratios (Ti/(Ti+Ta)) [22]. The authors showed that Ti doping, in particular cation ratios around 0.2 - 0.3, promotes structural homogeneity at the nearest-neighbor level which seems to correlate with low mechanical loss. In their study the film with the lowest mechanical loss (cation ratio of 0.283) was also the least oxygen deficient, suggesting that Ti doping might prevent oxygen loss. On follow up work Bassiri *et. al.* found that annealing of the films did not greatly affect the structure, only subtle changes in the short-order were observed, but proposed that the medium range order could show significant changes as a function of the annealing temperature. Modeling and experiments in zirconia doped tantala have confirmed that modifications in the medium range order that result in more corner sharing tetrahedra favors low room temperature mechanical loss in that mixture [23]. However, modeling of room temperature mechanical loss is specially challenging as most models struggle with accurately reproducing experimental results particularly the dependence on the cation concentration [24–27].

Herein we report the results of a detailed study of the evolution in the atomic structure, morphology, optical properties and mechanical loss of reactively sputtered titania-doped tantala upon annealing. It is shown that for a dopant cation concentration of 0.27, the annealing process induces atomic mixing leading to the formation of a titania-tantala compound. The crystallized phase identified after annealing at 750°C is indexed as $TiTa_{18}O_{47}$. Instead, the film with a higher cation concentration of 0.53 is phase separated with only the titania crystallizing at 500°C. At an annealing temperature of 600°C, where the structural modifications are clearly identified, the titania-doped tantala films with cation ratio of 0.27 achieves the lowest mechanical loss and absorption loss at the laser interferometer wavelength of 1064 nm. At these conditions, the films are less dense than the as-deposited film due to the presence of Ar-filled voids. In combination, these results show, for the first time, that the lowest mechanical loss is associated with a material morphology that consists of an atomically homogenous mixed titanium-tantalum oxide containing a low density of nanometer sized Ar-filled voids.

2. Experimental

2.1. Film deposition

The titania-doped tantala films with cation ratio of 0, 0.27, 0.53 and 1 films were deposited by reactive biased target deposition (RBTD) [28,29] using the LANS system manufactured by 4Wave, Inc. The RBTD technique involves the use of a low energy ion source that generates an Ar ion plume that is directed at a negatively biased metallic target to sputter the target. The deposition system fits six 100 mm diameter metallic targets with a mobile shutter that exposes three targets at a time. Metallic targets are biased using an asymmetric, bipolar pulsed DC power

Optical Materials EXPRESS

supply. The same negative bias is applied to the exposed targets but the positive pulse width and period can be individually controlled. For mixed films the Ti and Ta targets were operated simultaneously but the individual pulse widths were varied to realize different mixture proportions of the materials while the pulse period was fixed at 100 μs. The O_2 flow was optimized for each deposition condition in order to optimize optical properties. The base pressure was 1×10^{-7} Torr while the process pressure was around 6×10^{-4} Torr. The pulse width at which the Ta/Ti targets were biased to achieve the desired composition, and deposition conditions evaluated in this work are presented in Table 1. The deposition rates of the films ranged from 0.004 - 0.02 nm/s. The dopant cation ratio was obtained from the elemental concentrations determined by x-ray photoelectron spectroscopy.

Table 1. Deposition conditions and dopant cation concentration ratios obtained from XPS for the films evaluated in this work. In all cases, the pulse repetition rate was 100 μs.

Film	O_2 flow (sccm)	Target	Pulse width (μs)	Deposition rate (nm/s)	Dopant cation ratio
I	14	Ta	2	0.02091 ± 0.00005	0
II	12	Ti/Ta	2 / 53	0.01603 ± 0.00005	0.27 ± 0.04
III	8	Ti/Ta	2 / 82	0.00731 ± 0.00003	0.53 ± 0.06
IV	12	Ti	2	0.00397 ± 0.00001	1

Film thickness was kept around 200 - 250 nm for tantala and titania-doped tantala films and around 120 nm for titania films. Coatings were grown on Si (100) wafers for XPS measurements and on fused silica substrates of 25.4 mm diameter and 6.35 mm thick for the rest of the structural and optical characterization techniques employed. For mechanical loss measurements 75 mm diameter and 1 mm thick fused silica substrates were employed. Post-deposition annealing in air was carried out using a Fisher Scientific Isotemp programmable muffle furnace in which the temperature was increased at a rate of 100°C per hour until a soaking temperature of 300°C, 500°C, 600°C, 650°C, 700°C and 750°C was reached. For each temperature a soaking time of 10 hours was used.

2.2. GIXRD measurements

Grazing incidence x-ray diffraction (GIXRD) measurements were carried out on a Bruker D8 Discover Series I diffractometer with a Cu Kα source. The incident angle was kept at 0.5° and 2θ was varied between 10° and 80°. In this configuration the x-ray intensity is 90% attenuated in a length of 340 nm of tantala and 720 nm of titania. Results for tantala and titania films are described in the Appendix section.

2.3. XPS measurements

X-ray photoelectron spectroscopy (XPS) measurements were performed using a Physical Electronics PE 5800 ESCA/ASE system equipped with a monochromatic Al Kα x-ray source. The photoelectron take-off angle was fixed at 45° and a charge neutralizer was used with a current of 10 μA for all measurements. The instrument base pressure was around 1×10^{-9} Torr. Spectra were analyzed using CasaXPS software (version 2.3.19) [30]. An in-depth analysis of XPS data is described in the Appendix.

2.4. TEM and EELS measurements

transmission electron microscopy (TEM) and electron energy loss spectroscopy (EELS) measurements were performed by Eurofins Materials Science. The samples were prepared using the *in situ* focused ion beam (FIB) lift out technique on a FEI Strata 400 Dual Beam FIB/SEM. The samples were imaged with a FEI Tecnai TF-20 FEG/TEM operated at 200 kV in bright-field TEM mode

Optical Materials EXPRESS

and high-angle annular dark-field scanning transmission electron microscopy (STEM/HAADF) mode.

2.5. Optical measurements

Optical characterization of the films was realized by spectroscopic ellipsometry along with measurements of absorption loss at λ = 1064 nm and transmittance spectrophotometry. Ellipsometric data were collected at an angle of incidence of 60° using a Horiba UVISEL ellipsometer in a spectral range of 0.59 eV to 6.5 eV. The fitting of spectroscopic ellipsometry data was performed using the DeltaPsi2 software. Several dispersion models for the materials were evaluated to obtain film thickness, refractive index and extinction coefficient. From the dispersion of the extinction coefficient, the energy band gap was estimated by the Tauc method [31] for indirect transitions and further verified by the Cody method [32] when the range of linear dependency could not be determined unambiguously from the Tauc plot. The Appendix section describes the analysis of these results. Absorption loss was measured at λ = 1064 nm by photothermal common path interferometry [33]. For each sample five spots were measured in the surface within a 4 mm × 4 mm area.

2.6. Mechanical loss measurements

Mechanical loss measurements were performed at the LIGO Laboratory (Caltech) using a gentle nodal suspension system [34,35] for as deposited films and after annealing at different temperatures. In all cases, various resonant modes were measured in a frequency range of 1 - 22 kHz.

3. Results

GIXRD results for titania-doped tantala films with different cation ratio concentrations are presented in Fig. 1. The as-deposited film with a cation dopant concentration of 0.27 shows an amorphous structure with broad features comparable to those observed for tantala (see Fig. 8(A) of the Appendix). These broad features are unchanged up to an annealing temperature of 600°C. However, the main broad feature around 2θ = 16 - 40° is sharper and higher in intensity after annealing at 700°C, which is indicative of the onset of the film crystallization. In fact, annealing to 750°C reveals peaks superimposed over the main broad features which indicate partial crystallization of the film. The peaks of the crystallized structure correspond to $TiTa_{18}O_{47}$ (reference pattern PDF 00-021-1423 [36]). This compound was observed in powder samples consisting of a mixture of tantala and titania in varying concentrations [37]. These previous XRD measurements are reported in a limited angular range, 2θ = 50° [23], which do not permit indexing of three peaks observed at higher positions in the diffractograms of Fig. 1(A). The crystal system of $TiTa_{18}O_{47}$ was identified as monoclinic. The relative intensities of the peaks match fairly well with the tabulated values except for a peak expected at 2θ = 30.03° which is not observed. This could be due to the peak being superimposed with the amorphous background still present or could also be indicative of texture in the structure. The cation ratio necessary to form $TiTa_{18}O_{47}$ is around 0.05 while the actual ratio of the film is much higher (0.27) so it is reasonable to expect that only a small portion of the amorphous layer has crystallized. Figure 1(B) presents the GIXRD spectra for the titania-doped tantala film with a dopant cation ratio of 0.53. The films as-deposited and annealed at 300°C indicate an amorphous structure with the broad features also observed for pure tantala and the mixed film with a lower dopant cation ratio. For an annealing temperature of 500°C two peaks centered at 2θ = (35.93 ± 0.03)° and 2θ = (53.9 ± 0.3)° appear, indicating that the film is partially crystallized. For the following annealing temperature of 600°C the diffractogram consists mainly of sharp peaks with only a broad feature remaining associated with the substrate. The peaks correspond to the titania rutile structure with a preferential orientation in the [101] direction. There are also significant shifts in peak

Optical Materials EXPRESS

positions that can be linked to a variation in lattice parameters, as there are no clear indications of the presence of residual stress in the film. In this case, one of the constituents of the mixture, titania, fully crystallizes while the tantala remains amorphous featuring a clear phase separation in the material. Remarkably, annealing this film at temperatures higher than the crystallization temperature of pure tantala (up to 850°C) does not induce crystallization of the tantala phase.

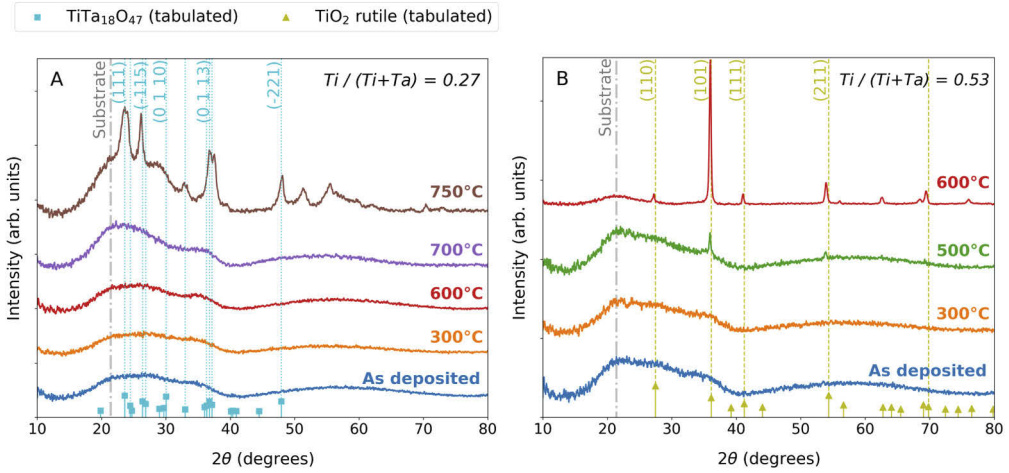

Fig. 1. Diffractograms for (A) titania-doped tantala film with a cation ratio = 0.27 and (B) titania-doped tantala film with a cation ratio = 0.53 as a function of annealing temperature. The fused silica substrate peak position is indicated in (A) and (B) with its main feature being a broad peak centered around $2\theta = 21°$. Tabulated peak positions for the $TiTa_{18}O_{47}$ compound and for titania in the rutile phase are included.

Annealing of the titania-doped tantala films also modified the material structure observed by XPS from the evolution of the Ta 4f and Ti 2p peaks. Figure 2(A) shows the variation of the Ta $4f_{7/2}$ peak position and the binding energy separation between the Ta doublet for tantala and titania-doped tantala films as a function of the annealing temperature. The position of the Ta $4f_{7/2}$ peak and the energy separation are well within the tabulated ranges for tantala [38–41] in all films at the different annealing temperatures. This indicates that the Ta oxidation state is that of tantala and that neither the annealing nor the dopant inclusion induce significant changes in the chemical environment of the Ta atoms.

A similar analysis for the Ti bonding environment in titania-doped tantala films is shown in Fig. 2(B). The Ti $2p_{3/2}$ peak position versus annealing for all films agrees with tabulated values for Ti(IV) oxidation state [38]. However, the energy separation of the doublet for the film with a cation ratio of 0.27 presents an interesting behavior. For the as deposited film the energy separation is in good agreement with the expected energy separation for Ti(IV). After annealing there is a significant increase of the doublet energy separation. Similar high values of energy separation have been reported for poorly oxidized titania films [42,43], but in this case the position of the O 1s and Ti $2p_{3/2}$ peaks do not correspond to a low oxidation state. This indicates that the chemical environment of the Ti atoms changes significantly with annealing up to the crystallization temperature and no longer corresponds to a titania environment, which could be indicative of an atomic mixture. After partial crystallization of the $TiTa_{18}O_{47}$ phase the energy separation is again within the range corresponding to Ti(IV), likely due to the fact that a large portion of the material remains amorphous in a tantala and a titania phase. For the titania-doped tantala film with a cation ratio of 0.53, the energy separation of the doublet components are consistent with Ti(IV) and do not show any marked dependency on the annealing temperature even after complete crystallization of the titania phase at 600°C. The energy separation measured after annealing

Optical Materials EXPRESS

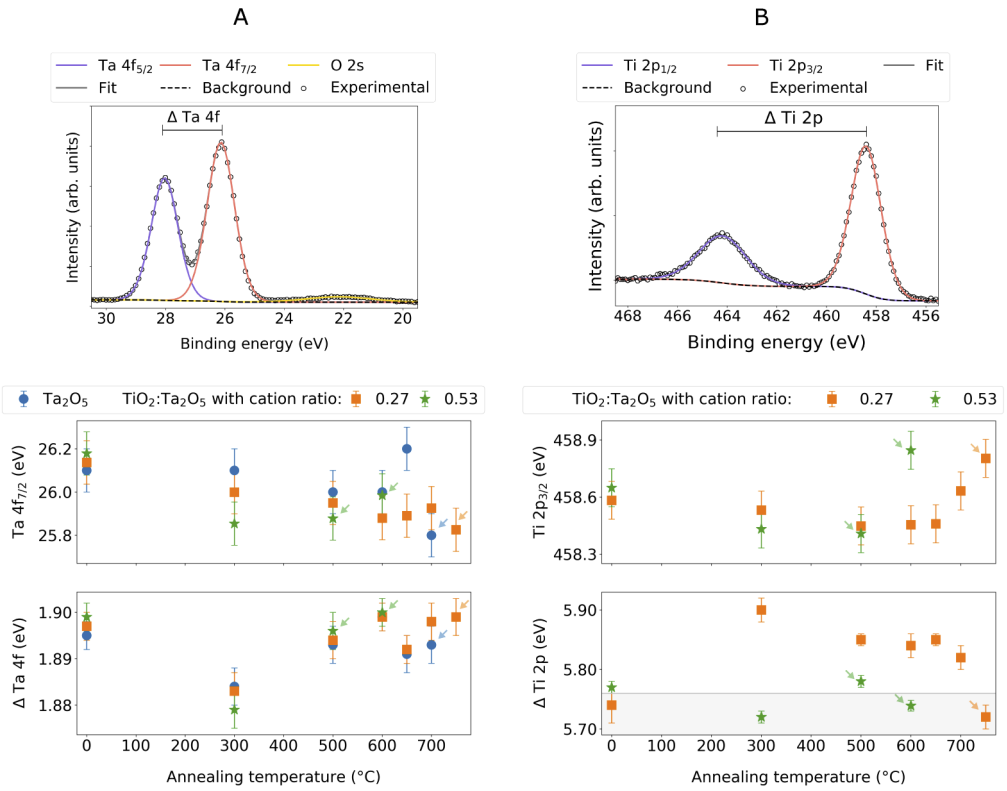

Fig. 2. XPS results for titania-doped tantala films. (A) Position of Ta $4f_{7/2}$ peak and energy separation of Ta 4f doublet. The position and peak separation for a tantala film are shown for reference. (B) Position of Ti $2p_{3/2}$ peak and energy separation of Ti 2p doublet in titania-doped tantala films. The shaded region indicates the tabulated values of energy separation for Ti(IV). Arrows indicate crystallized films as determined by the presence of sharp peaks in the diffractograms.

at 500°C is only deviated by 1σ from the tabulated values, which is not statistically significant. This indicates that the Ti atoms are in a titania chemical environment in the as-deposited films and after annealing, regardless of its structure being amorphous or partially crystallized.

Annealing of the titania-doped tantala films brings further structural modifications. Figure 3 shows TEM images of the cross section of tantala and titania-doped tantala films as deposited and after annealing at their corresponding highest temperatures before the onset of crystallization. As expected, the as-deposited films present a dense morphology. After annealing both the tantala film and the mixed film with a cation ratio of 0.53 remain compact with no changes in the morphology within the resolution of the TEM images. However, the titania-doped tantala film with 0.27 cation concentration shows the presence of closed voids with a characteristic diameter of 1 – 2 nm and a surface density around 0.02 voids/nm^2, which are identified as dark regions in the STEM/HAADF image. These voids lead to a reduction of the packing density in the film. This is supported by the fact that the refractive index decreases and the film thickness increases with annealing temperature as shown in Fig. 4. The refractive index at $\lambda = 1064$ nm wavelength is reduced by almost 2% between the as deposited and annealed films and is accompanied by an increase in thickness of 7%. In contrast, both the tantala and titania-doped tantala with 0.53 cation ratio feature no statistically significant changes in the refractive index or thickness after annealing. An analysis of the refractive index by means of the Wiener bounds approach [44] (see

Optical Materials EXPRESS

Appendix) indicates that the packing density is reduced to (0.97 ± 0.02) while a reduction in the refractive index is expected only for voids larger than 1 nm, which is consistent with the void dimensions determined from the TEM images of Fig. 3(B). Void formation induced by annealing has been reported for other sputtered oxide thin films [12,45–47] but not for mixed films. In this case, the dopant cation ratio appears to be a key contributing factor to void formation. Even at lower annealing temperatures, the mixed film with 0.27 cation ratio already exhibits a clear increase in thickness in contrast with the tantala film and the mixed film with 0.53 cation ratio.

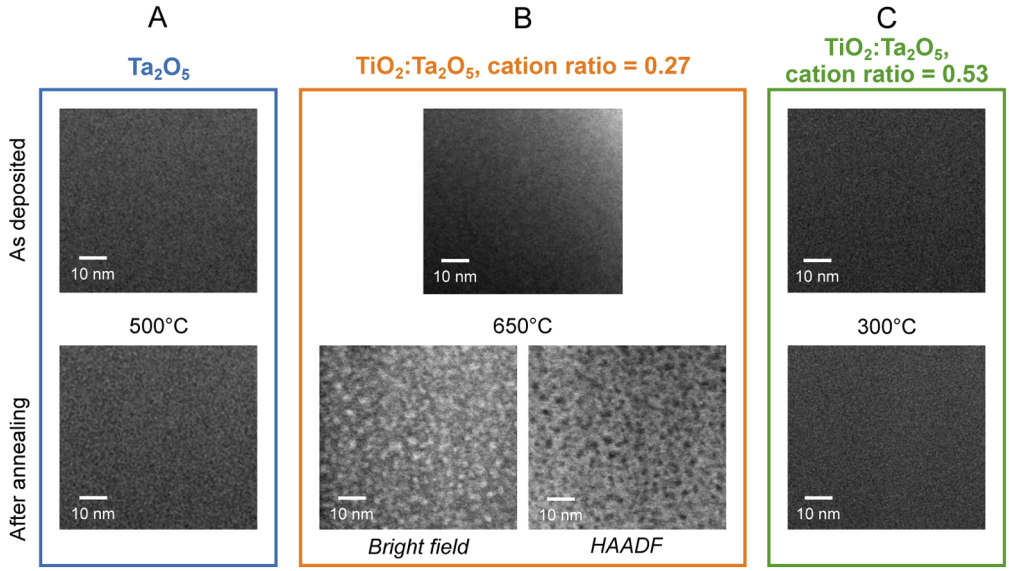

Fig. 3. TEM images for (A) tantala film, (B) titania-doped tantala film with a cation ratio = 0.27 and (C) titania-doped tantala film with a cation ratio = 0.53 as deposited and after annealing. All TEM images are bright field except otherwise specified.

EELS analysis for a titania-doped tantala film with a cation ratio = 0.27 after annealing show the voids are mostly filled with Ar, as can be observed in Fig. 5. The EELS spectra taken from a line profile across the surface show a distinct increase only in Ar concentration that correlates with the lowest intensity regions in the HAADF/STEM image. The atomic concentrations obtained by EELS should only be considered qualitatively as this is a standardless technique and for quantification careful calibration should be carried out. From previous RBS studies done in our group, IBS films typically feature 3 - 5% of Ar which is in good agreement with the detection of Ar by EELS in the film regardless of the presence of voids. During film deposition, Ar at a partial pressure around 4×10^{-6} Torr is used to operate the ion source. The entrapped Ar in the film can be due to chemisorbed Ar or implanted Ar reflected off the target. The elevated Ar concentration in the voids could be due to aggregation induced by the annealing process.

The effect of doping and annealing on the optical properties of the films was characterized. Table 2 summarizes the values of the refractive index at λ = 1064 nm, the optical band gap and absorption loss at λ = 1064 nm normalized to a thickness of 250 nm for the as-deposited films and after annealing at the highest temperature before crystallization. For tantala the refractive index and band gap agree well with reported values for films grown by reactive sputtering [48]. The refractive indices of the mixed films follow the expected scaling with Ti doping. The dispersion of refractive index, $n(\lambda)$, and extinction coefficient, $k(\lambda)$, for all as deposited films are shown in Fig. 6. $n(\lambda)$ in Fig. 6(B) is shown for wavelengths at which $k(\lambda)$ is negligible. It can be observed that the refractive index dispersion for the mixed films cannot be completely reproduced as a

Optical Materials EXPRESS

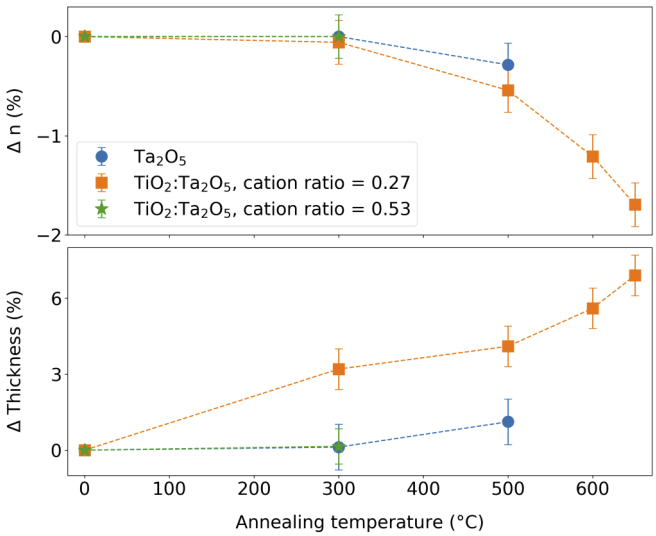

Fig. 4. Variation of the refractive index at λ = 1064 nm and of the thickness of tantala and titania-doped tantala films as a function of the annealing temperature before the onset of crystallization. Note that tantala and titania-doped tantala with a cation ratio of 0.53 after annealing at 300°C present similar variations in refractive index and thickness and thus the data points are superimposed.

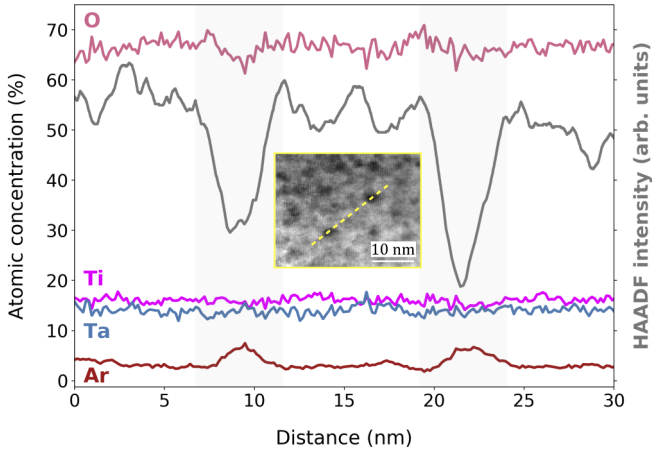

Fig. 5. TEM/EELS line profile of a titania-doped tantala film with a cation ratio = 0.27 after annealing at 650°C and its corresponding HAADF intensity. Gray shaded zones correspond to voids as determined by a lower HAADF intensity. Inset shows the HAADF/STEM image where the line profile was measured. Atomic concentrations are not accurate due to the lack of standards of EELS.

linear combination of the dispersions of tantala and titania as has been suggested in a previous work [17]. For titania-doped tantala with a cation ratio of 0.27, a comparison of the extinction coefficient and refractive index as a function of wavelength for the coating as deposited and after annealing at 650°C is also presented in Fig. 6.

The absorption loss at λ = 1064 nm for tantala and titania-doped tantala with a cation ratio of 0.27 is in the parts per million for as-deposited films and reduces upon annealing. This results in

Optical Materials EXPRESS

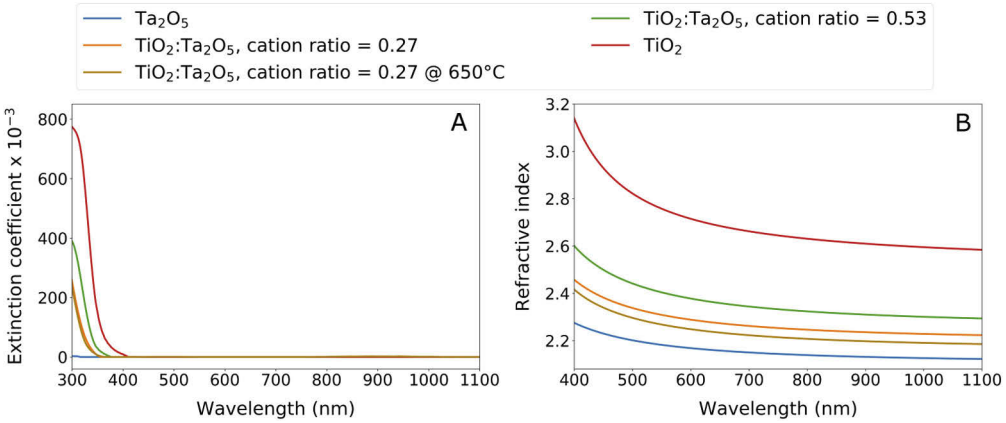

Fig. 6. (A) Extinction coefficient and (B) refractive index as a function of wavelength. Data correspond to tantala as deposited, titania as deposited, titania-doped tantala with a cation ratio of 0.27 as deposited and after annealing at 650°C and titania-doped tantala with a cation ratio of 0.53 as deposited.

Table 2. Refractive index at λ = 1064 nm and optical band gap estimation for the as deposited films. The absorption loss at λ = 1064 nm normalized to a thickness of 250 nm is given for as deposited and annealed films. In all cases the extinction coefficient remains below 1×10^{-4} for all wavelengths > 350 nm. Values for the absorption loss of titania film which is crystalline as deposited are excluded.

Film	n at λ = 1064 nm	Optical band gap (eV)	Absorption loss at λ = 1064 nm (ppm)	
			As deposited	Annealed
Ta_2O_5	2.12 ± 0.01	4.12 ± 0.06	5.7 ± 0.3	5.0 ± 0.2
Ta_2O_5:TiO_2, cation ratio = 0.27	2.22 ± 0.01	3.47 ± 0.04	8.1 ± 0.3	3.9 ± 0.3
Ta_2O_5:TiO_2, cation ratio = 0.53	2.30 ± 0.01	3.39 ± 0.04	79.5 ± 0.6	18.6 ± 0.4
TiO_2	2.59 ± 0.01	3.28 ± 0.05	-	-

part from reduction of the concentration of oxygen defects in the thin films due to the annealing process [49,50]. In particular, for the tantala film, the decrease in absorption can be associated with an increase of around 8% in the lattice oxygen proportion as determined by XPS (see Appendix). In fact, in the current state-of-the-art coatings for gravitational wave interferometers, the absorption loss was reduced from 0.7 ppm to 0.25 ppm when the tantala layers of the mirrors were replaced by titania-doped tantala [20].

Dopant cation ratio and annealing also have a profound impact in the mechanical loss of the coatings. The coating loss angle at a frequency around 1 kHz as a function of annealing temperature for tantala and titania-doped tantala films is presented in Fig. 7. For an as-deposited tantala coating the loss angle is $(9.7 \pm 0.9) \times 10^{-4}$ and reduces to $(4.7 \pm 0.3) \times 10^{-4}$ after annealing at 500°C, in good agreement with reported values [17,21]. The loss angle for the as deposited titania-doped tantala films is lower than for tantala, around $6.9 - 7.2 \times 10^{-4}$. After annealing at 500°C the loss angle for both doped films is decreased and remains lower than that of tantala. However, after annealing at 600°C, the loss angle of the film with a cation ratio of 0.53 increases to $(13 \pm 1) \times 10^{-4}$. In contrast, the titania-doped tantala film with a cation ratio of 0.27 shows a marked decrease reaching a value of $(2.8 \pm 0.3) \times 10^{-4}$ which is roughly a reduction of 40% in the loss angle compared to the annealed tantala film. This reduction is comparable to previously reported values for titania-doped tantala with a dopant concentration around 20% grown by ion beam sputtering (IBS) [14–21]. It is relevant to point out that at 600°C the 0.27 cation ratio

Optical Materials EXPRESS

titania-doped tantala reaches lower values of the loss angle and the absorption loss at 1064 nm than any of the other films in this study.

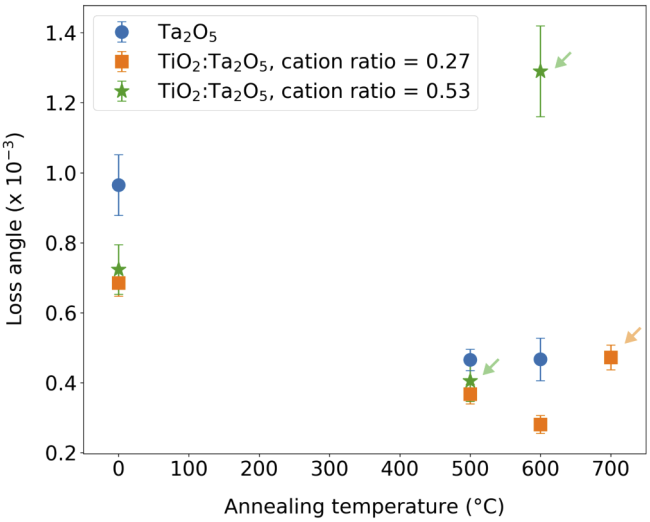

Fig. 7. Coating loss angle at 1 kHz for a tantala film and titania-doped tantala films with dopant cation ratio of 0.27 and 0.53 as a function of the annealing temperature. Arrows indicate crystallized films as determined by the presence of sharp peaks in the diffractograms.

4. Discussion and conclusions

The results of the characterization of titania-doped tantala thin films presented in the previous section provide valuable insight into the structural modifications that occur with annealing and doping. In tantala films, there is an 8% increase in the lattice oxygen concentration upon annealing that suggests that oxygen rearrangement induced by the thermal treatment is taking place. This oxygen rearrangement occurs while the structure of the film remains amorphous. Although the changes in the absorption loss and refractive index at $\lambda = 1064$ nm, or the band gap are minimal, the oxygen rearrangement decreases mechanical loss.

The addition of titania to tantala adds other variables that influence the properties of the materials that strongly depend on dopant concentration. For the highest 0.53 cation ratio the as-deposited films are a mixture of tantala and titania and thus a phase separated material. Beyond 500°C titania crystallizes in its rutile phase while tantala remains amorphous. This is consistent with previous reports that showed elevated titania concentrations can lead to phase separation in sol-gel films [51]. The mechanical loss of the as-deposited film is lower than for a tantala film but it reaches a similar value after annealing at 500°C. The high absorption loss at $\lambda = 1064$ nm for the as-deposited film may indicate a lack of oxygen, which is partially compensated by annealing at atmospheric conditions, but not sufficiently to reduce the absorption loss to parts per million as in tantala.

The titania-doped tantala film with a cation ratio of 0.27 shows the most significant structural modifications with annealing. The material evolves from a mixture of tantala and titania to an atomically homogenous ternary compound after annealing up to 650°C. This is evidenced by the fact that the chemical environment of the Ti atoms is no longer consistent with a titania configuration. This supports previous research that suggested that tantala and titania are mixed at the atomic scale [22,51]. Moreover, the ternary compound $TiTa_{18}O_{47}$ crystallizes after annealing at 700°C. The thermal treatment also induces the formation of Ar-filled voids with a characteristic

Optical Materials EXPRESS

diameter of 1 – 2 nm and a surface density around 0.02 voids/nm^2. This effect has not been previously reported for the mixed oxide films but was suggested as a possible cause for the measured variation in the Young's modulus of a 25% titania-doped tantala film [52]. Similar features referred to as Ar bubbles were reported in a tantala film grown by IBS by MacLaren *et. al.* [53], and by Harthcock *et. al.* in IBS HfO_2 films [54]. Recent simulation efforts indicate that the presence and distribution of voids might contribute significantly to the coating loss angle of the material [27]. Jiang *et. al.* studied zirconia doped tantala and found that annealing not only promotes homogeneity by modifying the chemical environment of the Zr atoms but also allows for a homogenous distribution of voids, resulting in decreased mechanical loss. The voids reported in that study, however, are smaller than the ones found in titania-doped tantala as the size of the simulation system is roughly a 2 nm box and thus cannot reproduce nanometer sized voids. Further studies are needed to elucidate the role of voids in the loss angle of the mixed oxide coatings.

In combination, the results conclusively show that the atomic mixing of titania and tantala and the formation Ar-filled voids upon annealing in titania-doped tantala with a cation ratio of 0.27 result in a material that has the minimum coating loss angle and absorption loss at λ = 1064 nm. Higher Ti cation ratio leads to phase separation which in turn increases mechanical loss. Therefore a path towards identifying promising mixed amorphous oxide thin films with low mechanical loss would need to account for the thermodynamics of ternary phase formation that could promote atomic mixing. A high crystallization temperature alone might not predictive of low mechanical loss and dopant cation ratio should be kept low to avoid phase separation in the film.

Appendix

GIXRD measurements of tantala and titania films

GIXRD measurements of tantala and titania thin films deposited by reactive ion beam sputtering are shown in Fig. 8. The structure of the tantala film remains amorphous up to an annealing temperature of 600°C and after annealing at 700°C the film is crystallized, which is consistent with previous reports of IBS tantala films [55]. The diffraction peaks correspond to the β-tantala structure (reference pattern PDF 00-025-0922 [36]). Figure 8(B) shows the diffractogram for a titania film which, in sharp contract with the tantala film, is crystallized as deposited and the structure is consistent with rutile (reference pattern PDF 00-021-1276 [36]). The substrate peak is more pronounced due to the lower thickness of this film and the increased X-ray penetration depth for titania compared to that of tantala.

Detail of XPS measurements and analysis

The XPS measurements include survey spectra collected at a pass energy of 188 eV, 0.8 eV step, 30 s sweep intervals and a total of 20 sweeps and high resolution spectra obtained using a 23.5 eV pass energy, 0.1 eV step and 100 s sweep intervals. Table 3 presents the atomic concentrations determined by XPS of all the elements detected in the as deposited film surface.

Table 3. Atomic concentrations obtained by XPS for the films as deposited.

Film	Atomic concentrations (%)			
	C	O	Ta	Ti
Ta_2O_5	30 ± 3	48 ± 2	22 ± 1	-
Ta_2O_5:TiO_2, cation ratio = 0.27	29 ± 3	50 ± 2	15.4 ± 0.9	5.7 ± 0.4
Ta_2O_5:TiO_2, cation ratio = 0.53	30 ± 3	49 ± 2	10.0 ± 0.6	11.3 ± 0.7
TiO_2	51 ± 6	38 ± 2	-	11.3 ± 0.5

Optical Materials EXPRESS

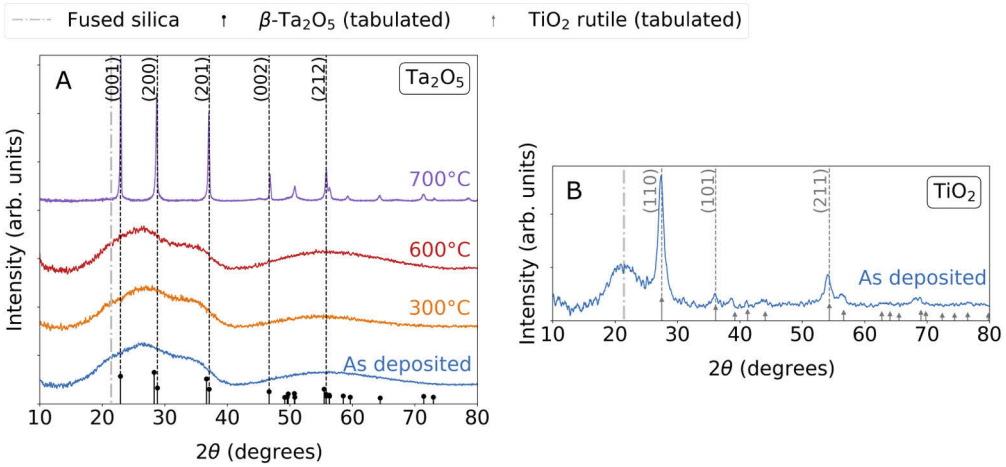

Fig. 8. Diffractograms for (A) a tantala film and (B) a titania film as a function of annealing temperature. The fused silica substrate peak position is indicated in (A) and (B) with its main feature being a broad peak centered around $2\theta = 21^\circ$. Tabulated peak positions for β-Ta_2O_5 and for titania in the rutile phase are included.

High resolution measurements were carried out for relevant spectral lines of each element: C 1s, O 1s, Ta 4f and Ti 2p for all films at the different annealing temperatures. All peaks were fit with a lineshape of a Gaussian Lorentzian product form with a mixing factor of 30 [39].

The position of the adventitious carbon peak obtained from the fit was used to calibrate the binding energy scale of the high resolution spectra for each analyzed sample. This shift introduces an uncertainty of ± 0.1 eV in the peak positions [56]. As a result, the uncertainty on peak positions has two contributions: from this calibration procedure and from the fitting, while the uncertainty on energy separation between peaks takes into consideration the contribution from the peak fit only and therefore is much lower leading to more precise determination of energy separation values. The O 1s peak has two components: lattice and non-lattice oxygen. For the tantala film and the titania film the lattice and non-lattice peak positions are in good agreement with reported values for these compounds [38–41]. The percentage of lattice oxygen, calculated as the ratio of the lattice oxygen peak area to the total O 1s peak area, shows an increase for the tantala film of 8% after the first annealing step at 300°C and remains constant for the rest of the annealing temperatures. No suboxide or metallic tantalum peaks were found and O 1s shows no presence of oxygen bonded to tantala in a lower oxidation state which should present as an asymmetry to lower energies [57]. Residuals obtained from the fits of Ti 2p indicate no presence of additional peaks, which implies that the expected Ta 4p peak has very low intensity and has been included as part of the Shirley background.

Wiener bounds approach

For a binary dielectric mixture, several mixing models exist to describe the effective dielectric function (ϵ) of the mixed material. These models make different assumptions about the host material and the inclusions, in particular the shape of the inclusions given by their depolarization factor (L). However, the models converge to the same expression in two limiting cases: $L = 0$ and $L = 1$, which can be regarded as upper and lower limits for the effective dielectric function of the mixture independent of its topology. Using that $n(\lambda) = \sqrt{\epsilon(\lambda)}$ the bounds for the refractive index of a mixture are [44]:

$$n_u(\lambda, p_u) = \sqrt{p_u n_H^2(\lambda) + (1 - p_u) n_L^2(\lambda)} \tag{1}$$

Optical Materials EXPRESS

$$n_l(\lambda, p_l) = \frac{n_L(\lambda) n_H(\lambda)}{\sqrt{p_u n_H^2(\lambda) + (1 - p_u) n_L^2(\lambda)}} \tag{2}$$

where n_u, n_l are the upper and lower bounds for the refractive index of the mixture respectively, n_L, n_H the refractive indices of the low and high index components of the mixed film and p_u, p_l the upper and lower bounds for the volume filling factor of the high index component. The procedure to obtain the Wiener bounds is to plot the dispersion for the mixed film along with the upper and lower bounds given by Eqs. (1) and (2) respectively. To estimate the upper bound p_u is decreased from 1 until n_u matches the measured dispersion at any wavelength. For the lower bounds, p_l is increased from 0 until n_l matches the measured dispersion at any wavelength. This procedure can only be applied in the range of wavelengths for which the absorption is negligible. For estimating the packing density the inclusions are assumed to have refractive index equal to 1, which is a good approximation for Ar in the frequency range of the analysis, and the volume filling fraction obtained corresponds to the filling fraction of the solid component often called the packing density.

Band gap estimation

The dispersion of refractive index, $n(\lambda)$, and extinction coefficient, $k(\lambda)$, and the optical band gap of the coatings were studied by spectroscopic ellipsometry. From $k(\lambda)$, the typical Tauc plot shown in Fig. 9 was constructed to determine the optical bandgap. There are no significant variations in the optical band gap of the tantala films and titania-doped tantala film with a cation ratio of 0.27 after annealing. In the case of the titania-doped tantala film with a cation ratio of 0.53 the band gap decreases to (3.22 ± 0.07) eV after annealing at 600°C (when the rutile phase is crystallized). This value is in good agreement with that of the titania film that features a crystalline rutile structure.

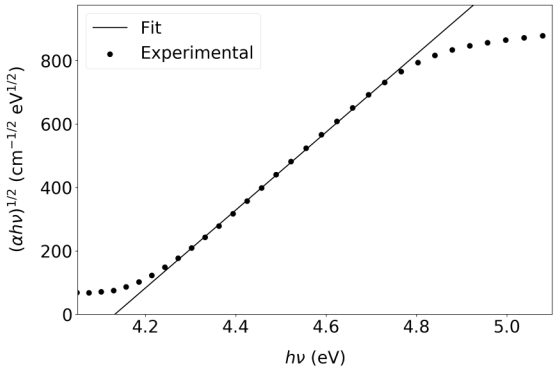

Fig. 9. Typical Tauc plot for an as-deposited tantala film. The estimated optical band gap is (4.12 ± 0.06) eV.

TEM/EELS compositional map of a titania-doped tantala film with cation ratio = 0.27 after annealing at 650° C

Figure 10 shows TEM/EELS compositional maps and its corresponding HAADF/STEM image of a titania-doped tantala film with a cation ratio = 0.27 after annealing at 650°C. It can be observed that the voids (dark regions in the HAADF/STEM image) correlate with Ar-rich regions.

Optical Materials EXPRESS

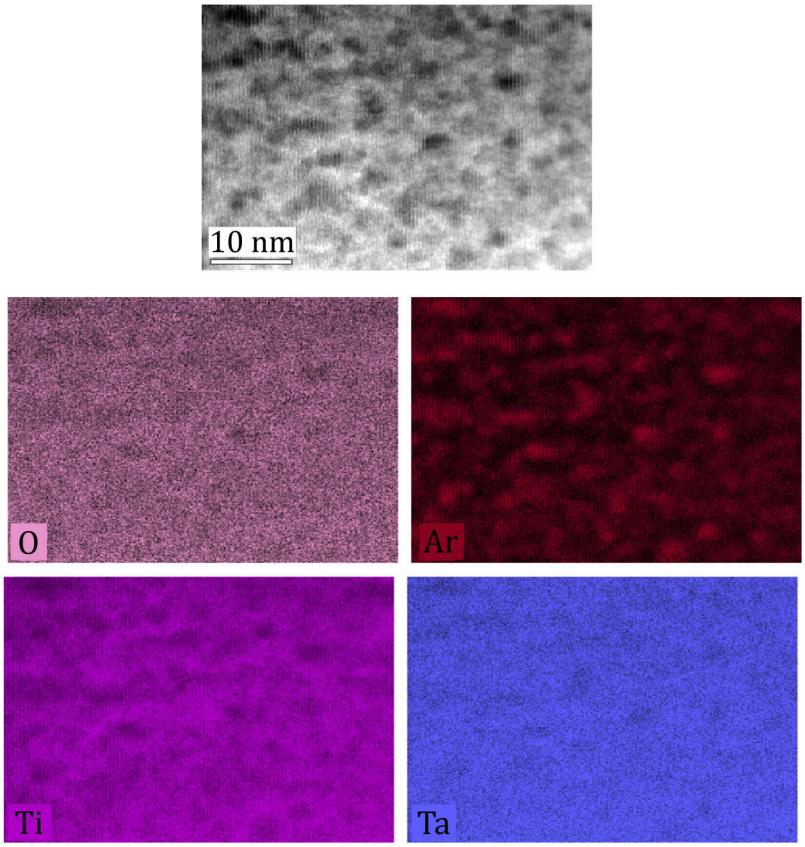

Fig. 10. TEM/EELS compositional maps and its corresponding HAADF/STEM image of a titania-doped tantala film with a cation ratio = 0.27 after annealing at 650°C.

Funding

National Science Foundation Moore Foundation Center for Coatings Research (1710957).

Disclosures

The authors declare no conflicts of interest.

References

1. P. R. Saulson, "Thermal noise in mechanical experiments," Phys. Rev. D **42**(8), 2437–2445 (1990).
2. K. Numata, A. Kemery, and J. Camp, "Thermal-noise limit in the frequency stabilization of lasers with rigid cavities," Phys. Rev. Lett. **93**(25), 250602 (2004).
3. A. D. Ludlow, T. Zelevinsky, G. K. Campbell, S. Blatt, M. M. Boyd, M. H. G. de Miranda, M. J. Martin, J. W. Thomsen, S. M. Foreman, J. Ye, T. M. Fortier, J. E. Stalnaker, S. A. Diddams, Y. Le Coq, Z. W. Barber, N. Poli, N. D. Lemke, K. M. Beck, and C. W. Oates, "Sr lattice clock at 1× 10–16 fractional uncertainty by remote optical evaluation with a ca clock," Science **319**(5871), 1805–1808 (2008).
4. T. Rosenband, D. Hume, P. Schmidt, C.-W. Chou, A. Brusch, L. Lorini, W. Oskay, R. E. Drullinger, T. M. Fortier, and J. E. Stalnaker, "Frequency ratio of Al+ and Hg+ single-ion optical clocks; metrology at the 17th decimal place," Science **319**(5871), 1808–1812 (2008).
5. M. Bishof, X. Zhang, M. J. Martin, and J. Ye, "Optical spectrum analyzer with quantum-limited noise floor," Phys. Rev. Lett. **111**(9), 093604 (2013).
6. LIGO Scientific Collaboration and Virgo Collaboration, "Gw150914: The advanced LIGO detectors in the era of first discoveries," *Phys. Rev. Lett.* 116(13), 131103 (2016).

Optical Materials EXPRESS

7. F. Acernese, M. Agathos, K. Agatsuma, D. Aisa, N. Allemandou, A. Allocca, J. Amarni, P. Astone, G. Balestri, G. Ballardin, F. Barone, J.-P. Baronick, M. Barsuglia, A. Basti, F. Basti, T. S. Bauer, V. Bavigadda, M. Bejger, M. G. Beker, C. Belczynski, D. Bersanetti, A. Bertolini, M. Bitossi, M. A. Bizouard, S. Bloemen, M. Blom, M. Boer, G. Bogaert, D. Bondi, F. Bondu, L. Bonelli, R. Bonnand, V. Boschi, L. Bosi, T. Bouedo, C. Bradaschia, M. Branchesi, T. Briant, A. Brillet, V. Brisson, T. Bulik, H. J. Bulten, D. Buskulic, C. Buy, G. Cagnoli, E. Calloni, C. Campeggi, B. Canuel, F. Carbognani, F. Cavalier, R. Cavalieri, G. Cella, E. Cesarini, E. Chassande-Mottin, A. Chincarini, A. Chiummo, S. Chua, F. Cleva, E. Coccia, P.-F. Cohadon, A. Colla, M. Colombini, A. Conte, J.-P. Coulon, E. Cuoco, A. Dalmaz, S. D'Antonio, V. Dattilo, M. Davier, R. Day, G. Debreczeni, J. Degallaix, S. Deléglise, W. D. Pozzo, H. Dereli, R. D. Rosa, L. D. Fiore, A. D. Lieto, A. D. Virgilio, M. Doets, V. Dolique, M. Drago, M. Ducrot, G. Endrőczi, V. Fafone, S. Farinon, I. Ferrante, F. Ferrini, F. Fidecaro, I. Fiori, R. Flaminio, J.-D. Fournier, S. Franco, S. Frasca, F. Frasconi, L. Gammaitoni, F. Garufi, M. Gaspard, A. Gatto, G. Gemme, B. Gendre, E. Genin, A. Gennai, S. Ghosh, L. Giacobone, A. Giazotto, R. Gouaty, M. Granata, G. Greco, P. Groot, G. M. Guidi, J. Harms, A. Heidmann, H. Heitmann, P. Hello, G. Hemming, E. Hennes, D. Hofman, P. Jaranowski, R. J. G. Jonker, M. Kasprzack, F. Kéfélian, I. Kowalska, M. Kraan, A. Królak, A. Kutynia, C. Lazzaro, M. Leonardi, N. Leroy, N. Letendre, T. G. F. Li, B. Lieunard, M. Lorenzini, V. Loriette, G. Losurdo, C. Magazzù, E. Majorana, I. Maksimovic, V. Malvezzi, N. Man, V. Mangano, M. Mantovani, F. Marchesoni, F. Marion, J. Marque, F. Martelli, L. Martellini, A. Masserot, D. Meacher, J. Meidam, F. Mezzani, C. Michel, L. Milano, Y. Minenkov, A. Moggi, M. Mohan, M. Montani, N. Morgado, B. Mours, F. Mul, M. F. Nagy, I. Nardecchia, L. Naticchioni, G. Nelemans, I. Neri, M. Neri, F. Nocera, E. Pacaud, C. Palomba, F. Paoletti, A. Paoli, A. Pasqualetti, R. Passaquieti, D. Passuello, M. Perciballi, S. Petit, M. Pichot, F. Piergiovanni, G. Pillant, A. Piluso, L. Pinard, R. Poggiani, M. Prijatelj, G. A. Prodi, M. Punturo, P. Puppo, D. S. Rabeling, I. Rácz, P. Rapagnani, M. Razzano, V. Re, T. Regimbau, F. Ricci, F. Robinet, A. Rocchi, L. Rolland, R. Romano, D. Rosińska, P. Ruggi, E. Saracco, B. Sassolas, F. Schimmel, D. Sentenac, V. Sequino, S. Shah, K. Siellez, N. Straniero, B. Swinkels, M. Tacca, M. Tonelli, F. Travasso, M. Turconi, G. Vajente, N. van Bakel, M. van Beuzekom, J. F. J. van den Brand, C. V. D. Broeck, M. V. van der Sluys, J. van Heijningen, M. Vasúth, G. Vedovato, J. Veitch, D. Verkindt, F. Vetrano, A. Viceré, J.-Y. Vinet, G. Visser, H. Vocca, R. Ward, M. Was, L.-W. Wei, M. Yvert, A. Z. żny, and J.-P. Zendri, "Advanced virgo: a second-generation interferometric gravitational wave detector," Classical Quantum Gravity **32**(2), 024001 (2015).
8. H. B. Callen and R. F. Greene, "On a theorem of irreversible thermodynamics," Phys. Rev. **86**(5), 702–710 (1952).
9. Y. Levin, "Internal thermal noise in the LIGO test masses: A direct approach," Phys. Rev. D **57**(2), 659–663 (1998).
10. S. D. Penn, P. H. Sneddon, H. Armandula, J. C. Betzwieser, G. Cagnoli, J. Camp, D. R. M. Crooks, M. M. Fejer, A. M. Gretarsson, G. M. Harry, J. Hough, S. E. Kittelberger, M. J. Mortonson, R. Route, S. Rowan, and C. C. Vassiliou, "Mechanical loss in tantala/silica dielectric mirror coatings," Classical Quantum Gravity **20**(13), 2917–2928 (2003).
11. I. W. Martin, R. Bassiri, R. Nawrodt, M. Fejer, A. Gretarsson, E. Gustafson, G. Harry, J. Hough, I. MacLaren, and S. Penn, "Effect of heat treatment on mechanical dissipation in Ta_2O_5 coatings," Classical Quantum Gravity **27**(22), 225020 (2010).
12. R. P. Netterfield, M. Gross, F. N. Baynes, K. L. Green, G. M. Harry, H. Armandula, S. Rowan, J. Hough, D. R. Crooks, and M. M. Fejer, "Low mechanical loss coatings for LIGO optics: progress report," in *Advances in Thin-Film Coatings for Optical Applications II*, vol. 5870 (International Society for Optics and Photonics, 2005), p. 58700H.
13. G. Vajente, R. Birney, A. Ananyeva, S. Angelova, R. Asselin, B. Baloukas, R. Bassiri, G. Billingsley, M. Fejer, and D. Gibson, "Effect of elevated substrate temperature deposition on the mechanical losses in tantala thin film coatings," Classical Quantum Gravity **35**(7), 075001 (2018).
14. M. Granata, E. Saracco, N. Morgado, A. Cajgfinger, G. Cagnoli, J. Degallaix, V. Dolique, D. Forest, J. Franc, C. Michel, L. Pinard, and R. Flaminio, "Mechanical loss in state-of-the-art amorphous optical coatings," Phys. Rev. D **93**(1), 012007 (2016).
15. M. Granata, A. Amato, L. Balzarini, M. Canepa, J. Degallaix, D. Forest, V. Dolique, L. Mereni, C. Michel, L. Pinard, B. Sassolas, J. Teillon, and J. Cagnoli, "Amorphous optical coatings of present gravitational-wave interferometers," Classical Quantum Gravity **37**(9), 095004 (2020).
16. T. L. S. Collaboration, "Advanced LIGO," Classical Quantum Gravity **32**(7), 074001 (2015).
17. G. M. Harry, M. R. Abernathy, A. E. Becerra-Toledo, H. Armandula, E. Black, K. Dooley, M. Eichenfield, C. Nwabugwu, A. Villar, D. R. Crooks, and G. Cagnoli, "Titania-doped tantala/silica coatings for gravitational-wave detection," Classical Quantum Gravity **24**(2), 405–415 (2007).
18. R. Flaminio, J. Franc, C. Michel, N. Morgado, L. Pinard, and B. Sassolas, "A study of coating mechanical and optical losses in view of reducing mirror thermal noise in gravitational wave detectors," Classical Quantum Gravity **27**(8), 084030 (2010).
19. M. Principe, I. M. Pinto, V. Pierro, R. DeSalvo, I. Taurasi, A. E. Villar, E. D. Black, K. G. Libbrecht, C. Michel, N. Morgado, and L. Pinard, "Material loss angles from direct measurements of broadband thermal noise," Phys. Rev. D **91**(2), 022005 (2015).
20. S. Gras, H. Yu, W. Yam, D. Martynov, and M. Evans, "Audio-band coating thermal noise measurement for advanced LIGO with a multimode optical resonator," Phys. Rev. D **95**(2), 022001 (2017).
21. A. Amato, G. Cagnoli, M. Canepa, E. Coillet, J. Degallaix, V. Dolique, D. Forest, M. Granata, V. Martinez, and C. Michel, "High-reflection coatings for gravitational-wave detectors: State of the art and future developments," in *Journal of Physics: Conference Series*, vol. 957 (IOP Publishing, 2018), p. 012006.

Optical Materials EXPRESS

22. R. Bassiri, K. Evans, K. Borisenko, M. Fejer, J. Hough, I. MacLaren, I. Martin, R. Route, and S. Rowan, "Correlations between the mechanical loss and atomic structure of amorphous tio2-doped ta2o5 coatings," Acta Mater. **61**(4), 1070–1077 (2013).
23. K. Prasai, J. Jiang, A. Mishkin, B. Shyam, S. Angelova, R. Birney, D. Drabold, M. Fazio, E. Gustafson, G. Harry, S. Hoback, J. Hough, C. Lévesque, G. MacLaren, A. Markosyan, I. W. Martin, C. S. Menoni, P. G. Murray, S. Penn, S. Reid, R. Robie, S. Rowan, F. Schiettekatte, R. Shink, A. Turner, G. Vagente, H.-P. Cheng, M. M. Fejer, A. Mehta, and R. Bassiri, "High precision detection of change in intermediate range order of amorphous zirconia-doped tantala thin films due to annealing," Phys. Rev. Lett. **123**(4), 045501 (2019).
24. F. Puosi, F. Fidecaro, S. Capaccioli, D. Pisignano, and D. Leporini, "In silico broadband mechanical spectroscopy of amorphous tantala," Phys. Rev. Res. **1**(3), 033121 (2019).
25. T. Damart, E. Coillet, A. Tanguy, and D. Rodney, "Numerical study of the structural and vibrational properties of amorphous ta2o5 and tio2-doped ta2o5," J. Appl. Phys. **119**(17), 175106 (2016).
26. J. P. Trinastic, R. Hamdan, C. Billman, and H.-P. Cheng, "Molecular dynamics modeling of mechanical loss in amorphous tantala and titania-doped tantala," Phys. Rev. B **93**(1), 014105 (2016).
27. J. Jiang, A. Mishkin, K. Prasai, M. Yazback, R. Zhang, R. Bassiri, M. Fejer, and H.-P. Cheng, "Atomic structures modeling and mechanical loss study of amorphous zro2-doped ta2o5," unplublished work (2020).
28. V. Zhurin, H. Kaufman, J. Kahn, and T. Hylton, "Biased target deposition," J. Vac. Sci. Technol., A **18**(1), 37–41 (2000).
29. T. Hylton, B. Ciorneiu, D. Baldwin, O. Escorcia, J. Son, M. McClure, and G. Waters, "Thin film processing by biased target ion beam deposition," IEEE Trans. Magn. **36**(5), 2966–2971 (2000).
30. M. Fairley, *Casa Software Ltd*. (2005).
31. J. Tauc, R. Grigorovici, and A. Vancu, "Optical properties and electronic structure of amorphous germanium," Phys. Status Solidi B **15**(2), 627–637 (1966).
32. G. Cody, B. Brooks, and B. Abeles, "Optical absorption above the optical gap of amorphous silicon hydride," Sol. Energy Mater. **8**(1-3), 231–240 (1982).
33. A. Alexandrovski, M. Fejer, A. Markosian, and R. Route, "Photothermal common-path interferometry (pci): new developments," in *Solid State Lasers XVIII: Technology and Devices*, vol. 7193 (International Society for Optics and Photonics, 2009), p. 71930D.
34. E. Cesarini, M. Lorenzini, E. Campagna, F. Martelli, F. Piergiovanni, F. Vetrano, G. Losurdo, and G. Cagnoli, "A "gentle" nodal suspension for measurements of the acoustic attenuation in materials," Rev. Sci. Instrum. **80**(5), 053904 (2009).
35. G. Vajente, A. Ananyeva, G. Billingsley, E. Gustafson, A. Heptonstall, E. Sanchez, and C. Torrie, "A high throughput instrument to measure mechanical losses in thin film coatings," Rev. Sci. Instrum. **88**(7), 073901 (2017).
36. S. Gates-Rector and T. Blanton, "The powder diffraction file: a quality materials characterization database," Powder Diffr. **34**(4), 352–360 (2019).
37. J. Waring and R. Roth, "Effect of oxide additions on the polymorphism of tantalum pentoxide (system ta20s-ti02)," J. Res. Natl. Bur. Stand., Sect. A **72A**(2), 175 (1968).
38. National Institute of Standards and Technology, Gaithersburg MD, 20899, *NIST X-ray Photoelectron Spectroscopy Database, NIST Standard Reference Database Number 20* (2000). Doi:.
39. H. Demiryont, J. R. Sites, and K. Geib, "Effects of oxygen content on the optical properties of tantalum oxide films deposited by ion-beam sputtering," Appl. Opt. **24**(4), 490–495 (1985).
40. R. Simpson, R. G. White, J. F. Watts, and M. A. Baker, "Xps investigation of monatomic and cluster argon ion sputtering of tantalum pentoxide," Appl. Surf. Sci. **405**, 79–87 (2017).
41. E. Atanassova and D. Spassov, "X-ray photoelectron spectroscopy of thermal thin Ta_2O_5 films on Si," Appl. Surf. Sci. **135**(1-4), 71–82 (1998).
42. S. Haukka, E. L. Lakomaa, O. Jylha, J. Vilhunen, and S. Hornytzkyj, "Dispersion and distribution of titanium species bound to silica from titanium tetrachloride," Langmuir **9**(12), 3497–3506 (1993).
43. A. Platau, L. Johansson, A. Hagström, S.-E. Karlsson, and S. Hagström, "Oxidation of cerium and titanium studied by photoelectron spectroscopy," Surf. Sci. **63**, 153–161 (1977).
44. O. Stenzel, *The physics of thin film optical spectra* (Springer, 2015).
45. M. Tilsch, V. Scheuer, and T. T. Tschudi, "Effects of thermal annealing on ion-beam-sputtered sio 2 and tio 2 optical thin films," in *Optical Thin Films V: New Developments*, vol. 3133 (International Society for Optics and Photonics, 1997), pp. 163–176.
46. J. T. Brown, "Center wavelength shift dependence on substrate coefficient of thermal expansion for optical thin-film interference filters deposited by ion-beam sputtering," Appl. Opt. **43**(23), 4506–4511 (2004).
47. A. J. Waldorf, J. Dobrowolski, B. T. Sullivan, and L. Plante, "Optical coatings deposited by reactive ion plating," Appl. Opt. **32**(28), 5583–5593 (1993).
48. J. Ngaruiya, S. Venkataraj, R. Drese, O. Kappertz, T. Leervad Pedersen, and M. Wuttig, "Preparation and characterization of tantalum oxide films produced by reactive dc magnetron sputtering," Phys. Status Solidi A **198**(1), 99–110 (2003).
49. N. Kim and J. F. Stebbins, "Effects of annealing on the structure of ion beam sputtered amorphous tantalum oxide: Oxygen-17 MNR spectra and relaxation times," J. Non-Cryst. Solids **378**, 158–162 (2013).

Optical Materials EXPRESS

50. J. Ni, Q. Zhou, Z. Li, and Z. Zhang, "Oxygen defect induced photoluminescence of hf o 2 thin films," Appl. Phys. Lett. **93**(1), 011905 (2008).
51. N. Kim and J. F. Stebbins, "Structure of amorphous tantalum oxide and titania-doped tantala: 17o NMR results for sol–gel and ion-beam-sputtered materials," Chem. Mater. **23**(15), 3460–3465 (2011).
52. M. R. Abernathy, J. Hough, I. W. Martin, S. Rowan, M. Oyen, C. Linn, and J. E. Faller, "Investigation of the Young's modulus and thermal expansion of amorphous titania-doped tantala films," Appl. Opt. **53**(15), 3196–3202 (2014).
53. I. MacLaren, R. Cummings, and R. Bassiri, "Bubble characterisations using eels in Ta_2O_5," LIGO DCC *internal communication* G1900926 (2019).
54. C. Harthcock, S. Qiu, R. Negres, J. Hammons, T. Voisin, G. Guss, A. Martin, C. Stolz, M. Menor, and G. Bhowmik, "The impact of nano-bubbles on the laser performance of hafnia films deposited by oxygen assisted ion beam sputtering method," Appl. Phys. Lett. **115**(25), 251902 (2019).
55. R. P. Netterfield, "Csiro report 1: Ion beam deposited coatings," (2004). https://dcc.ligo.org/public/0027/T040236/000/T040236-00.pdf.
56. M. C. Biesinger, B. P. Payne, L. W. Lau, A. Gerson, and R. S. C. Smart, "X-ray photoelectron spectroscopic chemical state quantification of mixed nickel metal, oxide and hydroxide systems," Surf. Interface Anal. **41**(4), 324–332 (2009).
57. K. McNamara, O. Kolaj-Robin, S. Belochapkine, F. Laffir, A. Gandhi, and S. Tofail, "Surface chemistry and cytotoxicity of reactively sputtered tantalum oxide films on niti plates," Thin Solid Films **589**, 1–7 (2015).